

Review



Cite this article: Schouten D. 2018 Muon geotomography: selected case studies. *Phil. Trans. R. Soc. A* **377**: 20180061. <http://dx.doi.org/10.1098/rsta.2018.0061>

Accepted: 12 October 2018

One contribution of 22 to a Theo Murphy meeting issue 'Cosmic-ray muography'.

Subject Areas:

geophysics, high energy physics, particle physics

Keywords:

muon tomography, muon geotomography, geophysics

Author for correspondence:

Doug Schouten
e-mail: dschouten@crmgtm.com

Muon geotomography: selected case studies

Doug Schouten

CRM Geotomography Technologies, Inc., 4004 Wesbrook Mall,
Vancouver, Canada

 DS, 0000-0002-0452-6320

Muon attenuation in matter can be used to infer the average material density along the path length of muons underground. By mapping the intensity of cosmic ray muons with an underground sensor, a radiographic image of the overburden above the sensor can be derived. Multiple such images can be combined to reconstruct a three-dimensional density model of the subsurface. This article summarizes selected case studies in applying muon tomography to mineral exploration, which we call muon geotomography.

This article is part of the Theo Murphy meeting issue 'Cosmic-ray muography'.

1. Introduction

Muon radiography is a means of inferring average material density by measuring the attenuation of muons along a path length through matter. Muon tomography uses tomographic methods to derive three-dimensional density maps from multiple muon radiographic images.

Measurements of the muon intensity attenuation were first used by George [1] to measure the overburden of a railway tunnel, and by Alvarez *et al.* [2] in searches for hidden chambers within pyramids. More recently, muon radiography has been used in volcanology [3–7], in mineral exploration [8,9] and in various other industrial and security applications as summarized in [10].

Cosmic ray muons arise from high energy interactions between cosmic rays (primarily protons, alpha particles) and atoms in the Earth's atmosphere. Owing to their relatively high mass (compared to electrons) and long decay time, muons created in the upper atmosphere with energy larger than a few GeV have a high probability of surviving as they travel through air and even deep underground at nearly the speed of light. The flux of muons incident from all angles on the surface of the earth is about $1 \text{ cm}^{-2} \text{ min}^{-1}$ [11].

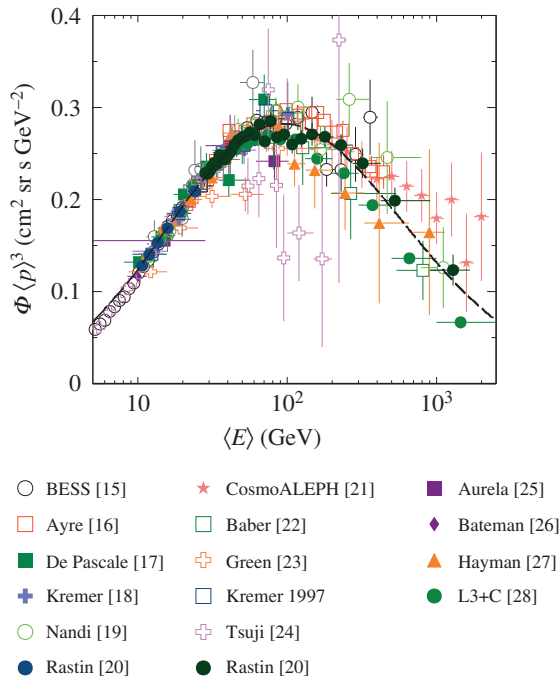


Figure 1. A global fit (dashed curve) of the vertical muon intensity versus muon energy at sea level, compared to a variety of datasets published from the 1960s to 2010s [15–28].

One heuristic model of the muon intensity at sea level is due to Gaisser [12]:

$$\frac{dN_\mu}{dE_\mu d\Omega dt dA} \approx \frac{0.14E_\mu^{-2.7}}{\text{GeV} \cdot \text{sr} \cdot \text{s} \cdot \text{cm}^2} \times \left(\frac{1}{1 + 1.1E_\mu \cos \theta / 115 \text{ GeV}} + \frac{0.054}{1 + 1.1E_\mu \cos \theta / 850 \text{ GeV}} \right), \quad (1.1)$$

where E_μ is the muon energy in GeV and θ is the zenith angle of the muon trajectory with respect to vertical. This model has been modified more recently by Tang *et al.* [13], and another model for the vertical muon flux has been proposed by Hebbeker & Timmermans [14]. We have combined these parameterizations in a global fit that takes more recent experimental data into account (figures 1 and 2).

Muons lose energy as they pass through matter via ionization, bremsstrahlung, pair production and other mechanisms at low energies [11,12]. Theoretical calculations for the various processes are well advanced (e.g. [11,29,30]) and have been implemented in a number of muon transport programs [31–34]. Interfacing the sea-level flux model with muon transport programs allows one to make precise predictions for the muon intensity I underground as a function of the opacity \mathcal{O} between the sensor and the surface, where opacity is defined as:

$$\mathcal{O} = \int_{\text{path}} \rho(x, y, z) d\ell. \quad (1.2)$$

In this definition, $\rho(x, y, z)$ is the three-dimensional distribution of underground density, and \mathcal{O} is in units of gram cm^{-2} , or metres of water equivalent (m w.e., hectogram cm^{-2}). Using the inverse

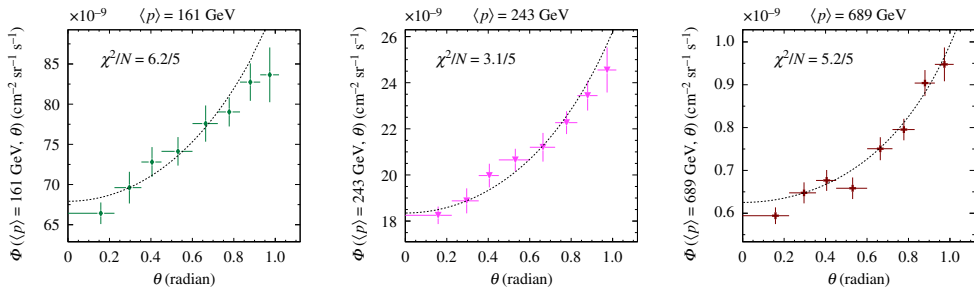


Figure 2. A global fit of muon intensity as a function of the zenith angle of the muon trajectory, compared to L3+C data [28] in three momentum ranges relevant to measurements of the cosmic ray muon intensity 100–500 m underground. Note that a flat scale factor is applied to the data (cf. figure 1) in all the momentum bins. (Online version in colour.)

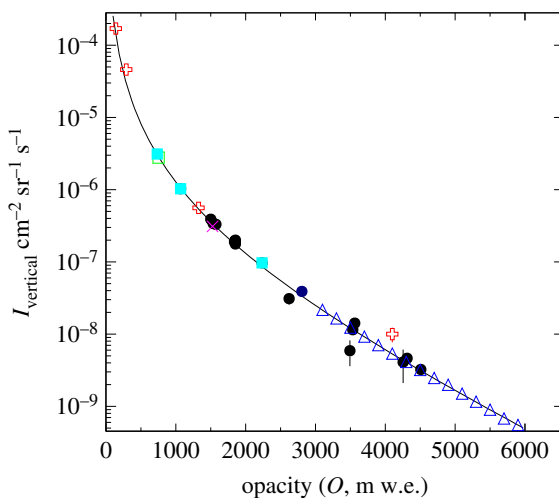


Figure 3. Vertical muon intensity versus opacity in units of metres of water equivalent (m w.e.), compared to a variety of datasets [35,36]. The theoretical model is for the standard rock composition defined in [12], and uses the muon physics simulation in Geant4 [32]. (Online version in colour.)

model I^{-1} , one is then able to infer an opacity \mathcal{O} from a measured I , and then one can calculate the average density along a given direction to the surface using

$$\langle \rho(x, y, z) \rangle = \frac{\mathcal{O}}{L}, \quad (1.3)$$

where $L = \int_{\text{path}} dl$ is the total path length to the surface in a particular direction. The relationship between muon intensity I and the overburden opacity \mathcal{O} is shown in figure 3.

2. Methodology

Using muon tracking sensors, trajectories for all muons passing through the sensor are measured and recorded. This allows one to generate maps of muon intensity, in which each pixel represents the measured intensity within a unit of solid angle. This intensity map can be compared to a reference map derived from an intensity model using *a priori* geological knowledge (for e.g. a reference assuming a simple uniform density distribution). For a given fixed muon intensity, the number of muons passing through the detector within an exposure time follows a Poisson distribution. A statistical interpretation of any deviations between the reference and measured

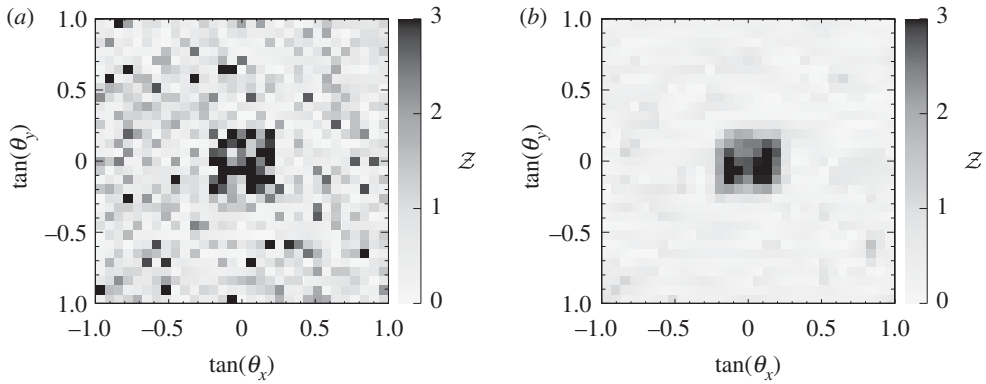


Figure 4. Synthetic radiographic images for a simulated $50\text{ m} \times 50\text{ m} \times 20\text{ m}$ cuboid (1 g cc^{-1} higher density than the surrounding ‘standard’ host rock with density 2.7 g cc^{-1}), 100 m above a muon sensor that is situated 400 m underground for 45 days. The images are shown with (a) and without (b) a sliding window filtering algorithm applied. See equation (2.2) for the definition of the image coordinates.

intensity in each pixel can, therefore be, determined by

$$p \equiv \left\{ \begin{array}{ll} \sum_{k=0}^N P(k; \lambda) & \text{if } N \geq \lambda \\ 1 - \sum_{k=0}^N P(k; \lambda) & \text{if } N < \lambda \end{array} \right\} \quad (2.1)$$

$$\mathcal{Z} \equiv \sqrt{2} \operatorname{erf}^{-1}(2p - 1) \cdot \operatorname{sgn}(\lambda - N),$$

and

where $\lambda = I_{\text{reference}} \times \Omega \cdot A_{\text{eff}} \cdot \Delta t$ is the expected number of muons from the reference model, P is the Poisson distribution function, N is the observed number of muons and \mathcal{Z} is the quantile of a standard normal distribution. Large positive values of \mathcal{Z} indicate a statistically significant higher opacity (lower intensity) unaccounted for in the reference geological model, whereas large negative values indicate a lower opacity (higher intensity). Images in which \mathcal{Z} is represented by a colour in each pixel are useful radiographic visualizations for identifying anomalous density within a muon sensor’s field of view. Examples of these images are shown in figure 4.

In all the case studies presented herein, muon tracking sensors based on segmented scintillators were used. These muon sensors are based on ‘super-planes’ of scintillator bars. Each super-plane consists of two planes of bars oriented in orthogonal directions. The length and width of each plane are either one by one metre or two by one metre, depending on the case study. The angular resolution of the sensors for muons with energy above 1 GeV is $10\text{--}13$ milliradians (depending on the muon angle), and the overall efficiency for identifying muons that pass through the detector, after applying all the reconstruction criteria, is greater than 90% in all cases. After reconstructing muon trajectories observed by a sensor, the set of muon angles are mapped to bins according to their respective directions in a rectilinear coordinate system

$$\left. \begin{array}{l} \tan \theta_x = \frac{\Delta x}{\Delta z} \\ \tan \theta_y = \frac{\Delta y}{\Delta z'} \end{array} \right\} \quad (2.2)$$

and

where x is east, y is north and z is depth such that $\tan \theta_x = \tan \theta_y = 0$ is pointing straight up to the surface. Each bin, or pixel, is therefore a pyramidal solid angle section from the detector to the surface of the earth.

In order to construct a three-dimensional density distribution from the muon tomography data, an inversion algorithm is used that minimizes a global function ϕ :

$$\min_{\rho(x,y,z)} \phi = \min_{\rho(x,y,z)} (\phi_D + \beta \cdot \phi_M), \quad (2.3)$$

where ϕ_D is a data misfit for the muon tomography data compared to the ideal reference model, and ϕ_M is a model objective function that ensures smoothness. These terms are defined as:

$$\phi_D = \sum_{i \in \text{pixels}} \frac{(d_i - \sum_j G_{ij} \rho_j)^2}{\sigma_i^2} \quad (2.4)$$

and

$$\phi_M = \sum_{w=x,y,z} \alpha_w \int_V \left(\frac{\partial \rho}{\partial w} \right)^{q_w} dV + \alpha_r \int_V (\rho_0 - \rho)^p dV, \quad (2.5)$$

where G_{ij} is the sensitivity of each i th pixel to the j th voxel in the image volume (note that G is a very sparse matrix), σ_i is the uncertainty of data measurement d_i , α_w is a constant that penalizes roughness in each of the $w = x, y, z$ coordinates and α_r is a constant that penalizes deviations from a reference model ρ_0 . Setting $\alpha_{r,x,y,z} = 0$ disables the respective parts of the model objective function. This method follows work by Oldenberg and Davis (Oldenburg D, Davis K and Kaminski V (2010), unpublished communication.) [37]. The exponents q_w and p are in the range (1, 2], with smaller values allowing for more complex (less smooth) models. The minimum of the global function ϕ is determined using the conjugate gradient minimization algorithm [38].

3. Case studies

(a) Myra falls

A proof of concept trial of muon geotomography was conducted in 2010 at the Nyrstar Myra Falls mine in British Columbia, Canada [8]. The Price deposit located at this mine is a volcanogenic massive sulfide (VMS) type deposit that contains zinc, copper, lead and silver. VMS deposits tend to have high-density contrast to the surrounding rock, and the Price deposit is particularly amenable to imaging with muon geotomography because it is only about 70 m below the surface, where the muon intensity is still quite high. Extensive drill core data for the Price deposit also allowed a detailed three-dimensional model of the density variation within the deposit. Using this drill data, radiographic images could be simulated to compare to the field data collected with a muon detector.

In the Myra Falls study, a single muon tracking sensor was exposed for about 15–20 days at seven different locations inside a mine tunnel below and off to the side of the Price deposit. The locations and fields of view of the detectors underneath the steep terrain are shown in figure 5. The surface topography model was created from LIDAR data. This was combined with a simple, reference geological model of uniform rock density $2.85 \text{ gram cm}^{-3}$ to predict the muon intensity at all angles up to 70 degrees from vertical, for each detector. The expected anomaly arising from the Price deposit was calculated by creating a second geological model that also contained the Price deposit three-dimensional density model, and then calculating the difference \mathcal{Z} (see equation (2.1)) of the predicted intensity from the simple reference model. The expected density anomaly in one of the radiographic images (from location ‘S5’) is shown in figure 6 along with the anomaly from field data, which is also calculated by comparison to the simple reference model. That the anomaly in the field data is spatially larger than expected is not surprising, because only the ore of economic value is assayed and can be incorporated in the simulation. In reality, most deposits are surrounded by altered rock that enhances their footprint.

One limitation encountered in this case study was that due to steep terrain and variable ground cover, the LIDAR data in a region around a crevasse on the mountainside was untrustworthy. This section of the radiographic images as depicted in figure 6 was excluded in the analysis.

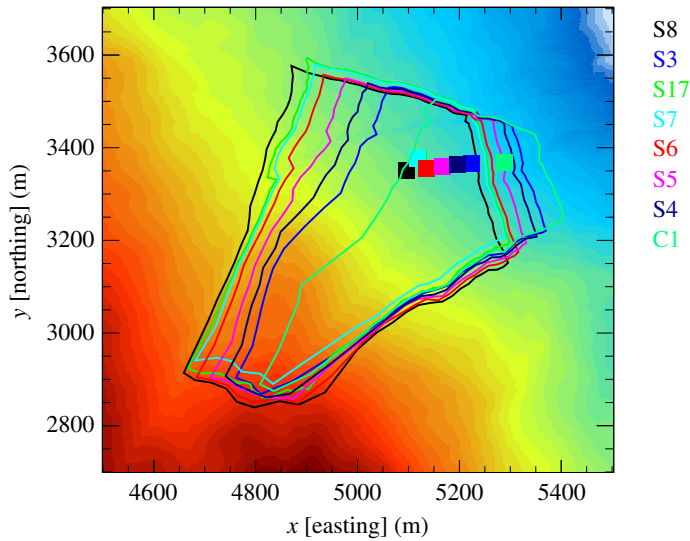


Figure 5. Surface topography above the Price deposit at the Myra Falls mine. The locations of the muon detectors (S3–S8, S17 and C1) along with their respective fields of view are denoted by the coloured squares. Note that location C1 is right at the entrance to the mine and was used for sensor calibration, not for imaging.

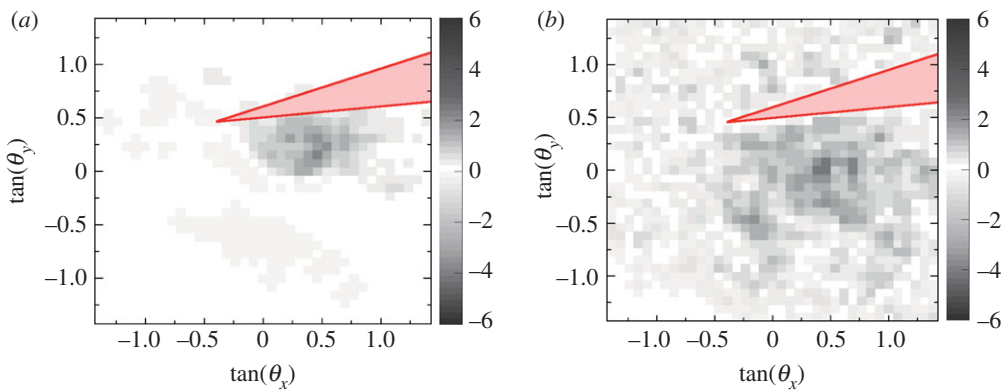


Figure 6. Expected muon radiograph at the S5 location for the Price deposit (a). The red shaded region of the image is excluded from the analysis due to untrustworthy surface topography. The measured muon radiograph is shown on (b). The measured anomaly is spatially larger than expected, as explained in the text. (Online version in colour.)

The remaining data from each of the sensor locations were used to invert for a 3D density distribution underground. In the inversion of muon data, no *a priori* geological information was used (i.e. $\alpha_r = 0$ in equation (2.5)). The comparison of the 3D model derived from muon geotomography measurements to the drill core data is shown in figure 7. This successful field trial is the first known application of muon geotomography to underground resource imaging.

(b) Pend Oreille

The Pend Oreille mine is located in northeastern Washington, USA. The MX700 deposit at about 450 m below surface is a Mississippi Valley-type (MVT) polymetallic (primarily lead and zinc) deposit with large density contrast to the surrounding dolomite. In this field trial, four detector locations were selected by the mine operator at about 540 m depth. Two muon tracking sensors

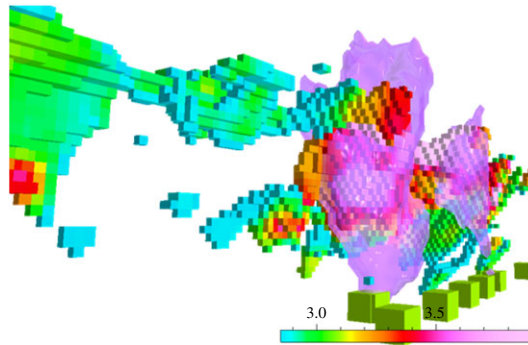


Figure 7. Isosurface of the three-dimensional density model derived by inverting the muon tomography data from the Myra Falls study. The density block model derived from drill core data for the Price deposit is also shown, as are the locations of the muon detector (not to scale) throughout the survey.

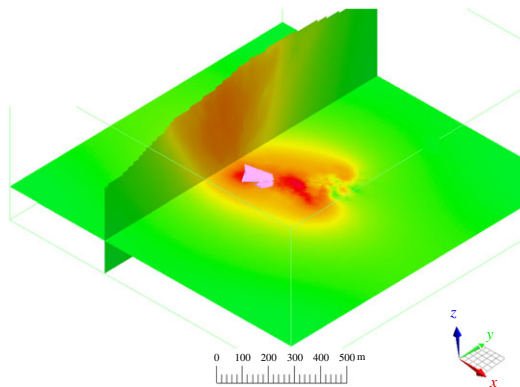


Figure 8. Vertical and horizontal slices through the three-dimensional density distribution derived from muon geotomography data in the Pend Oreille case study. The horizontal slice cuts through the ore shell model, also shown. The density is smeared out in depth, but follows the actual ore shell closely in the x – y coordinates.

were positioned at two of the locations each, and the sensors operated for 68–153 days at each location.

The muon geotomography survey at Pend Oreille was blind [9], in the sense that no information about the existence of the MX700 deposit nor any of its properties were revealed until the muon geotomography survey was completed. In the blinded analysis, the muon intensity measurements from each detector were inverted using the inversion methodology described above. The resultant three-dimensional model of underground density was provided to the mine operator and compared to the known geometry of the MX700 deposit. A comparison of the derived three-dimensional density model to the deposit ore shell model is shown in figure 8. Owing to the geometrical configuration of the survey, with the muon detectors directly below the deposit, the x – y reconstruction of the deposit shape follows the shell quite well, but the density model is smeared out in depth. This is because each two-dimensional radiographic image is sensitive to the average density along the entire muon path, or in other words, the position in z of an anomaly is poorly defined. This behaviour is a general feature of tomographic reconstruction of two-dimensional images: if the images of an object are all from approximately one side, the object geometry along the imaging direction is unconstrained.

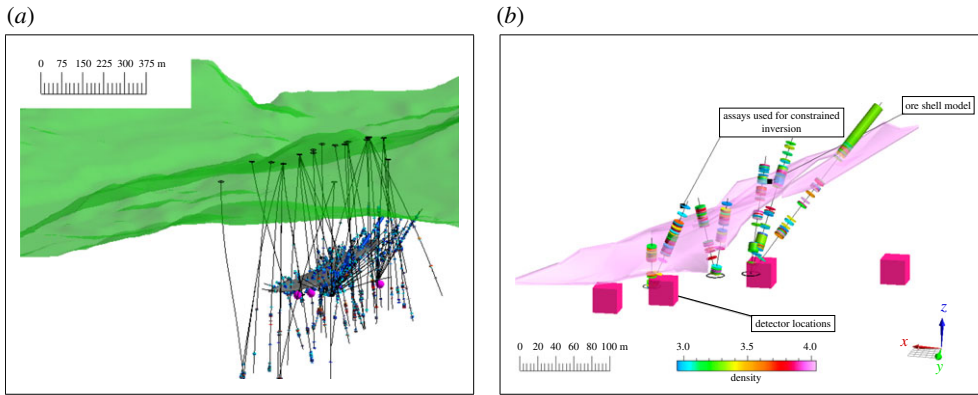


Figure 9. An overview of the drill holes with density assay information in and around the MX700 deposit (a). Most of the holes were started from locations in the mine underground. The five drill holes used in the joint inversion are shown (b) along with the density assays taken from core samples along the holes, in relation to the ore shell model.

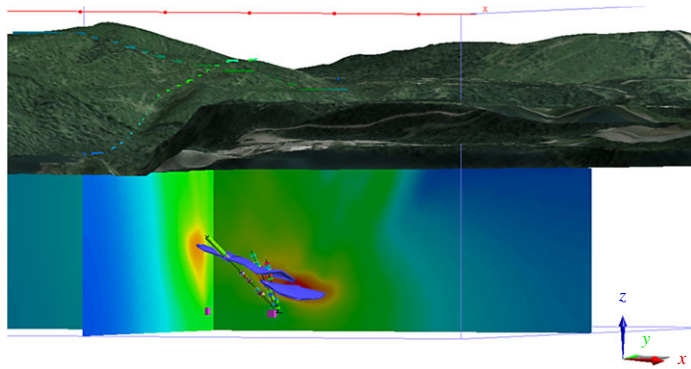


Figure 10. Vertical and horizontal slices through the three-dimensional density distribution derived from joint inversion of density assay and muon tomography data, shown along with the MX700 ore shell model. The variable surface topography and satellite imagery is also shown here.

Once the muon geotomography survey was completed, drilling data was incorporated in the analysis (figure 9). A joint inversion was performed that incorporated density assay information from five randomly selected drill holes (out of more than 250 available holes) in the data misfit term ϕ_D (see equation (2.3)). A term $((\rho_i - \rho_i^{\text{drill}})/\sigma_i)^2$ was added for each i th voxel intersected by a segment of logged drill core. The uncertainty σ_i on each assay measurement was assumed to be 5% of the measurement. Inclusion of a small set of direct density measurements in the inversion greatly constrains the geometry of the density distribution in the z -coordinate. The resultant three-dimensional density model from the joint inversion is shown in figure 10 and compared to the ore shell model.

(c) McArthur River

The McArthur River uranium deposit, discovered in 1988, is located approximately 500 m below the surface in the southeastern part of the Athabasca Basin in northern Saskatchewan, Canada. It is the richest and largest unconformity-related uranium deposit in the world, and accounts for about 10% of global production of uranium [39]. The mineralization occurs at depths between 500 m and 640 m around the unconformity. The deposit is not surrounded by an extensive

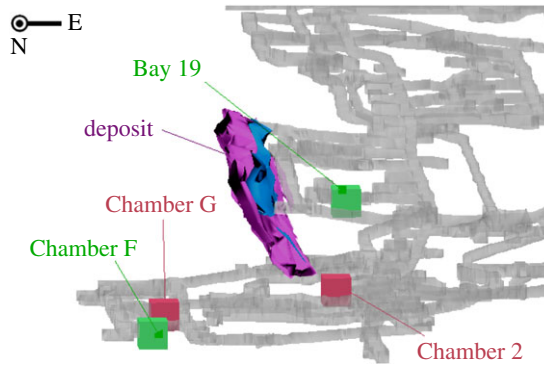


Figure 11. The McArthur River uranium deposit and the nearby mine workings. Also denoted are the locations of the muon tracking sensors used in the survey. Note the muon sensors depicted are not to scale. (Online version in colour.)

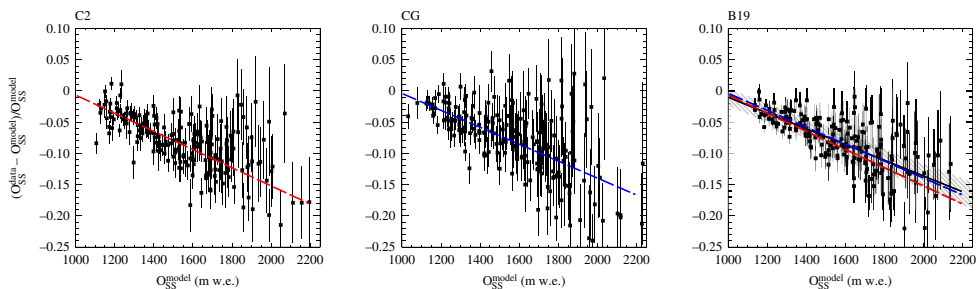


Figure 12. Relative difference between measured and modelled (expected) opacity, versus the modelled opacity from the sandstone only for Chamber 2, Chamber G and Bay 19 data, respectively. The same trend is observed in all the datasets but only the Bay 19 data are used to derive the correction. Comparison between the three trends is shown in the Bay 19 subfigure, along with the hatched area indicating the 68% uncertainty band around the fitted trend. (Online version in colour.)

alteration halo common to other unconformity associated uranium deposits [40,41], and therefore represents an interesting case study for imaging a very compact, dense ore body at depth.

Two muon tracking sensors were used in the survey, located at four distinct locations depicted as Chamber G, Chamber F, Chamber 2 and Bay 19 in figure 11. The configuration of sensors was chosen to optimize sensitivity and imaging capability, by providing views of the deposit from multiple locations and orientations, and to constrain the density of the sandstone using location Bay 19 above the deposit, since the muon intensity depends on the cumulative opacity along the muon path to the surface. A reference geological model was developed for the main geological units in the imaging volume (sandstone and basement metasedimentary gneisses) excluding the uranium deposit.

An unexpected global trend in the observed muon intensity versus depth was noted when the data were compared to the reference geological model. In order to isolate the analysis of the local geology around the deposit from the dominant sandstone units above the unconformity, the data from the sensor in Bay 19 were used to correct the opacity model for the sandstone *in situ*, as illustrated in figure 12. Owing to a paucity of drill data far from the deposit, the sandstone in the geological was treated uniformly as ‘standard’ rock [12], whereas density and chemical composition deviates throughout the sandstone overburden. Differences between the idealized rock and the actual sandstone can give rise to such an observed global trend, because greater than 80% of the opacity is comprised by the sandstone. Since the Bay 19 data are only sensitive to the sandstone above the deposit, they could be used to remove the global trend from

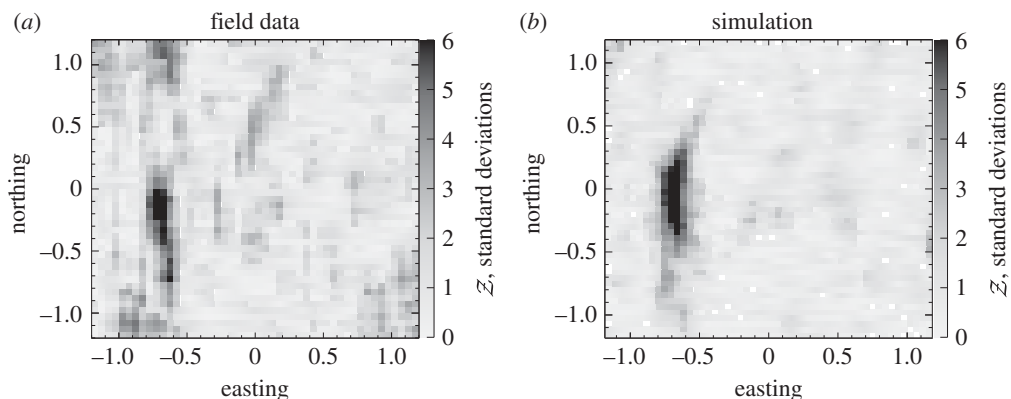


Figure 13. The anomalous Z for Chamber 2 data (a) from the McArthur River mine. Also shown for comparison is the same calculation for synthetic data (sampled from simulation, b). In both images, the same sliding-window filtering algorithm is applied. The x - and y -axes are $\tan(\theta_x)$ and $\tan(\theta_y)$ (see equation (2.2)), respectively.

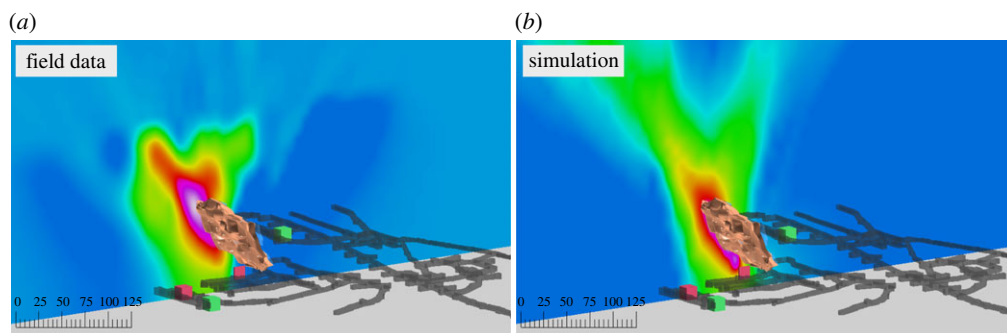


Figure 14. Slices through the density distribution derived by inverting actual (a) and synthetic (b) muon tomography data.

the other datasets in Chambers 2, G and F. This analysis illustrates the importance of judicious placement of muon sensors in areas where the local geology is unknown. By doing muon intensity measurements at multiple depths, a data-driven interpretation of a region of interest can be attained.

After correcting the global trend, a striking anomaly emerged in the muon data, as shown in figure 13. Comparison to the expected anomaly from simulation of the known deposit indicated good overall agreement between data and expectation. Differences between the simulation and data likely arise from the fact that the actual density distribution within the ore body is highly variable, whereas in the simulation, the deposit is modelled as uniform density. Comparison of the three-dimensional density inversion from muon data to the simulation is shown in figure 14.

4. Conclusion

Muon geotomography was first envisioned as a tool for resource exploration and monitoring by Malmqvist [42] in the 1970s, and is only now being realized due to advances in charged particle detector technology that allow for reliable and cost-effective measurements, as well as low-power, fast computing to facilitate automated muon track reconstruction in remote sensors. There are a number of compelling advantages for muon geotomography over other geophysical techniques, including insensitivity to EM and mechanical noise, continuously available and free signal source (cosmic rays), and directional imaging capability. The selected case studies

presented in this article have demonstrated the feasibility of detection and two-dimensional and three-dimensional imaging of dense ore bodies located hundreds of metres underground using muon geotomography. We expect that many applications for using cosmic ray muons to image large structures underground will be found within the next decades.

Data accessibility. This article has no additional data.

Competing interests. The author is an officer of CRM Geotomography Technologies, Inc., an incorporated company that builds and deploys muon detectors for resource exploration and monitoring.

Funding. I received no funding for this study.

References

1. George E. 1955 Cosmic rays measure overburden of tunnel. *Commonw. Eng.* 455–457.
2. Alvarez L *et al.* 1970 Search for hidden chambers in the pyramids using cosmic rays. *Science* **167**, 832–839. (doi:10.1126/science.167.3919.832)
3. Nagamine K, Iwasaki M, Shimomura K, Ishida. K. 1995 Method of probing inner-structure of geophysical substance with the horizontal cosmic-ray muons and possible application to volcanic eruption prediction. *Nucl. Instrum. Methods Phys. Res. Section A* **356**, 585–595. (doi:10.1016/0168-9002(94)01169-9)
4. Tanaka H *et al.* 2007 High resolution imaging in the inhomogeneous crust with cosmic-ray muon radiography: the density structure below the volcanic crater floor of Mt. Asama, Japan. *Earth Planet. Sci. Lett.* **263**, 104–113. (doi:10.1016/j.epsl.2007.09.001)
5. Ambrosi G *et al.* 2011 The MU-RAY project: volcano radiography with cosmic-ray muons. *Nucl. Instrum. Methods Phys. Res. Section A* **628**, 120–123. (doi:10.1016/j.nima.2010.06.299)
6. Marteau J, Gibert D, Lesparre N, Nicollin F, Noli P, Giacoppo. F. 2012 Muons tomography applied to geosciences and volcanology. *Nucl. Instrum. Methods Phys. Res. Section A* **695**, 23–28. (doi:10.1016/j.nima.2011.11.061)
7. Lesparre N, Gibert D, Marteau J, Komorowski J-C, Nicollin F, Coutant. O. 2012 Density muon radiography of La Soufriere of Guadeloupe volcano: comparison with geological, electrical resistivity and gravity data Muons tomography applied to geosciences and volcanology. *Geophys. J. Int.* **190**, 1008–1019. (doi:10.1111/j.1365-246X.2012.05546.x)
8. Bryman D, Bueno J, Oldenburg D, Liu Z. 2014 Bringing new physics to orebody imaging. Society of Economic Geologists Special Publication, vol. 18, pp. 235–241.
9. Bryman D, Bueno J, Jansen J. 2015 Blind test of Muon Geotomography for mineral exploration. In *ASEG Extended Abstracts*, vol. 164.
10. Checchia P. 2016 Review of possible applications of cosmic muon tomography. *J. Instrum.* **11**, C12072. (doi:10.1088/1748-0221/11/12/C12072)
11. Beringer J *et al.* 2012 Review of particle physics. *Phys. Rev. D* **86**, 010001. (doi:10.1103/PhysRevD.86.010001)
12. Groom D, Mokhov N, Striganov S. 2001 Muon stopping-power and range tables, 10 MeV–100 TeV. *Atomic Data Nuclear Data Tables* **78**, 183–356. (doi:10.1006/adnd.2001.0861)
13. Tang A, Horton-Smith G, Kudryavtsev V, Tonazzo A. 2006 Muon simulations for super-Kamiokande, KamLAND, and CHOOZ. *Phys. Rev. D* **74**, 053007. (doi:10.1103/physrevd.74.053007)
14. Hebbeker T, Timmermans C. 2002 A compilation of high energy atmospheric muon data at sea level. *Astroparticle Phys.* **18**, 107–127. (doi:10.1016/S0927-6505(01)00180-3)
15. Haino S *et al.* 2004 Measurements of primary and atmospheric cosmic-ray spectra with the BESS-TeV Spectrometer. *Phys. Lett. B* **594**, 35–46. (doi:10.1016/j.physletb.2004.05.019)
16. Ayre C, Baxendale J, Hume C, Nandi B, Thompson M, Whalley M. 1975 Precise measurement of the vertical muon spectrum in the range 20–500 GeV c^{-1} . *J. Phys. G Nucl. Phys.* **1**, 584–600. (doi:10.1088/0305-4616/1/5/010)
17. De Pascale M *et al.* 1993 Absolute spectrum and charge ratio of cosmic ray Muons in the energy region from 0.2 GeV to 100 GeV at 600 M above sea level. *J. Geophys. Res. Space Phys.* **98**, 3501–3507. (doi:10.1029/92ja02672)
18. Kremer J *et al.* 1999 Measurements of ground-level Muons at two geomagnetic locations. *Phys. Rev. Lett.* **83**, 4241–4244. (doi:10.1103/PhysRevLett.83.4241)

19. Nandi B, Sinha M. 1972 The momentum spectrum of Muons at sea level in the range 5–1200 GeV c⁻¹. *J. Phys. A Gen. Phys.* **5**, 1384–1394. (doi:10.1088/0305-4470/5/9/011)
20. Rastin B. 1984 An accurate measurement of the sea-level muon spectrum within the range 4–3000 GeV c⁻¹. *J. Phys. G Nucl. Phys.* **10**, 1609–1628. (doi:10.1088/0305-4616/10/11/017)
21. Grupen C *et al.* 2007 Cosmic ray results from the CosmoALEPH experiment. *Nucl. Phys. B Proc. Suppl.* **175–176**, 286–293. Proceedings of the XIV International Symposium on Very High Energy Cosmic Ray Interactions. (doi:10.1016/j.nuclphysbps.2007.11.014)
22. Baber S, Nash W, Rastin B. 1968 The momentum spectrum of muons at sea-level in the Range 3–1000 GeV c⁻¹. *Nucl. Phys. B* **4**, 539–548. (doi:10.1016/0550-3213(68)90112-0)
23. Green P, Duller N, Magnuson C, Choate L, Sheldon W, Osborne A, Benbrook J, Abdel-Monem M. 1979 Absolute intensities of medium-energy muons in the vertical and at Zenith angles 55°–85°. *Phys. Rev. D* **20**, 1598–1607. (doi:10.1103/PhysRevD.20.1598)
24. Tsuji S, Katayama T, Okei K, Wada T, Yamamoto I, Yamashita. Y. 1998 Measurements of muons at sea level. *J. Phys. G Nucl. Part. Phys.* **24**, 1805–1822. (doi:10.1088/0954-3899/24/9/013)
25. Aurela A, Wolfendale A. 1967 The energy spectrum of cosmic-ray muons in the vertical direction. *Ann. Acad. Sci. Fennicae A* **VI**, p. 225.
26. Bateman B, Cantrell W, Durda D, Duller N, Green P, Jelinek A, Nagy T, Sheldon W. 1971 Absolute measurement of the vertical cosmic ray muon intensity at 3–50 GeV c⁻¹ near sea level. *Phys. Lett. B* **36**, 144–148. (doi:10.1016/0370-2693(71)90130-4)
27. Hayman P, Wolfendale A. 1962 The momentum spectrum of cosmic ray muons near sea level in the momentum range 5–1000 GeV c⁻¹. *Proc. Phys. Soc.* **80**, 710–728. (doi:10.1088/0370-1328/80/3/315)
28. Achard P *et al.* 2004 Measurement of the atmospheric muon spectrum from 20–3000 GeV. *Phys. Lett. B* **598**, 15–32. (doi:10.1016/j.physletb.2004.08.003)
29. Kelner S, Kokoulin R, Petrukhin A. 1995 *About cross section for high-energy muon bremsstrahlung*. Moscow Inst. of Technology.
30. Kokoulin R, Petrukhin A. 1997 Muon interactions and consequences in underground physics. In *Proceedings of the Vulcano Workshop Frontier Objects in Astrophysics and Particle Physics*, p. 379.
31. Sokalski I, Bugaev E, Klimushin S. 2001 MUM: flexible precise Monte Carlo algorithm for Muon propagation through thick layers of matter. *Phys. Rev. D* **64**, 074015. (doi:10.1103/PhysRevD.64.074015)
32. Agostinelli S *et al.* 2003 Geant4—A simulation toolkit. *Nucl. Instrum. Methods Phys. Res. Section A* **506**, 250–303. (doi:10.1016/S0168-9002(03)01368-8)
33. Chirkin D, Rhode W. 2004 Propagating leptons through matter with Muon Monte Carlo (MMC). (<http://arxiv.org/abs/hep-ph/0407075>)
34. Kudryavtsev V. 2009 Muon simulation codes MUSIC and MUSUN for underground physics. *Comput. Phys. Commun.* **180**, 339–346. (doi:10.1016/j.cpc.2008.10.013)
35. Crouch M. 1987 An improved world survey expression for cosmic ray vertical intensity vs. depth in standard rock. In *Proc. Intl. Cosmic Ray Conf.*, p. 165.
36. Aglietta M *et al.* 2005 Muon ‘depth-intensity’ relation measured by the LVD underground experiment and cosmic-ray Muon spectrum at sea level. *Phys. Rev. D* **58**, 092005. (doi:10.1103/PhysRevD.58.092005)
37. Davis K, Oldenburg D. 2012 Joint 3D of muon tomography and gravity data to recover density. In *ASEG Extended Abstracts 2012: 22nd Geophysical Conf.*, pp. 1–4. (doi:10.1071/ASEG2012ab172)
38. Straeter TA. 1971 On the extension of the Davidon-Broyden class of rank one, quasi-newton minimization methods to an infinite dimensional Hilbert space with applications to optimal control problems. PhD thesis, North Carolina State University. NASA-CR-111975.
39. Bronkhurst D, Mainville AG, Murdock GM, Yesnik LD, Cameco Corporation. 2012 McArthur River Operation, Northern Saskatchewan, Canada. National Instrument 43-101 Technical Report.
40. Jefferson C *et al.* 2007 Unconformity-associated uranium deposits of the Athabasca Basin, Saskatchewan and Alberta. In *Mineral Deposits of Canada: a Synthesis of major deposit-types, district metallogeny, the evolution of geological provinces, and exploration methods*

- (ed. W Goodfellow), pp. 273–305. Geological Association of Canada, Mineral Deposits Division, Special Publication No. 5.
41. Jefferson C, Thomas D, Gandhi S, Ramaekers P, Delaney G, Brisbin D, Cutts C, Portella P, Olson R. 2007 Unconformity associated uranium deposits of the Athabasca basin, Saskatchewan and Alberta. In *Geological Survey of Canada, Bulletin*, vol. 588, pp. 23–67.
 42. Malmqvist L, Jönsson G, Kristiansson K, Jacobsson L. 1979 Theoretical studies of in-situ rock density determinations using underground cosmic-ray muon intensity measurements with application in mining geophysics. *Geophysics* **44**, 1549–1569. (doi:10.1190/1.1441026)